Colegio de Postgraduados

Calibration of forage maize plant cover using UAVs and satellite imagery in Google Earth Engine

Olivas-Rodríguez, Jesús A.[1]; Soto-Parra, Juan M.[1]; Jiménez-Jiménez, Sergio I.[2]; Marcial-Pablo, Mariana de J.[2]; Yáñez-Muñoz, Rosa M.[1]; Ponce-García, Omar C.[4]; Noperi-Mosqueda, Linda C.[1]; Ramírez-Valle, Orlando[3*]

[1] Universidad Autónoma de Chihuahua, Facultad de Ciencias Agrotecnológicas, Av. Pascual Orozco s/n, Campus 1, Santo Niño, Chihuahua, Chihuahua 31160, México
[2] Instituto Nacional de Investigaciones Forestales, Agrícolas y Pecuarias (INIFAP)—Centro Nacional de Investigaciones Disciplinarias sobre la Relación Agua-Suelo-Planta-Atmósfera (CENID-RASPA), Gómez Palacio 35079, Durango, México
[3] Instituto Nacional de Investigaciones Forestales, Agrícolas y Pecuarias (INIFAP), Campo Experimental La Campana-Sierra de Chihuahua, Aldama 32910, Chihuahua, México
[4] Instituto Nacional de Investigaciones Forestales, Agrícolas y Pecuarias (INIFAP), Campo Experimental Delicias, Delicias 33000, Chihuahua, México
* Correspondence: ramirez.orlando@inifap.gob.mx

Citation: Olivas-Rodríguez, J. A., Soto-Parra, J. M., Jiménez-Jiménez, S. I., Marcial-Pablo, M. de J., Yáñez-Muñoz, R. M., Ponce-García, O. C., Noperi-Mosqueda, L. C., & Ramírez-Valle, O. (2025). Calibration of forage maize plant cover using UAVs and satellite imagery in Google Earth Engine. *Agro Productividad*. https://doi.org/10.32854/9ax60p15

Academic Editor: Jorge Cadena Iñiguez
Associate Editor: Dra. Lucero del Mar Ruiz Posadas
Guest Editor: Daniel Alejandro Cadena Zamudio

Received: June 11, 2025.
Accepted: October 18, 2025.
Published on-line: December XX, 2025.

Agro Productividad, 18(11). November. 2025. pp: 247-262.

ABSTRACT

Objective: Estimate vegetation cover (VC) using Unmanned Aerial Vehicle (UAV) and Sentinel-2 satellite images for monitoring agricultural areas.

Design/methodology/approach: Sixteen vegetation indices (VI) were evaluated to automatically estimate VC. Observed VC was obtained from high-resolution georeferenced orthomosaics generated by a multispectral camera mounted on a UAV. These observed VC values were correlated with vegetation indices (VI) calculated from Sentinel-2 satellite imagery.

Results: The VIs with the best statistical performance in estimating VC were identified. It was found that the ARVI vegetation index can be used to accurately monitor VC for forage maize in Cuauhtémoc, Chihuahua.

Limitations/implications: The results obtained are representative of the specific conditions of the study area; however, their application in other regions requires prior calibration.

Findings/conclusions: Based on the coefficients obtained in this study, vegetation cover (VC) can be automatically monitored using the VICAL tool. This feature enables the monitoring of VC status across different plots and time periods during the agricultural cycle, facilitating spatial and temporal analysis of crop development.

Keywords: Remote sensing, vegetation cover, vegetation indices, VICAL.

INTRODUCTION

Vegetation cover (VC) is defined as the vertical projection area of vegetation elements onto the ground per unit of horizontal surface area (Gonsamo *et al.*, 2013). VC is also considered a key parameter in monitoring crop development, as it can be associated with

crop growth and evapotranspiration. This is because the dynamics of VC can reflect the phenological stages of crop growth (Calera, 2005). VC has been extensively used to evaluate the phenological and physiological status of vegetation, monitor crop development stages (Yu *et al.*, 2013), and estimate crop yields (Yang *et al.*, 2006).

Traditionally, VC is directly measured using quadrats, where a square frame is placed over the vegetation to assess plant density, cover, and frequency (Leirana-Alcocer & Bautista-Zúñiga, 2014). However, determining the precise moment when full cover is achieved is often complex and costly. Additionally, measuring VC in tall crops poses further challenges, prompting the frequent adoption of indirect methods (Alonso *et al.*, 2020).

High-resolution aerial imagery provides valuable spectral information on the radiation reflected by vegetation across various wavelengths (Torres-Sánchez *et al.*, 2014). To estimate VC using remote sensors, images captured by cameras mounted on Unmanned Aerial Vehicles (UAVs) can be employed and subsequently analyzed using vegetation indices (VIs) (Xiao & Moody, 2005).

In recent decades, the significant volume of remote sensing data, combined with advances in computational and image analysis technologies, has enabled extensive research on determining VC across large geographic scales—from regional to global levels (Jing *et al.*, 2006; Zhou & Lyu, 2016).

While the use of satellite imagery to derive vegetation indices offers considerable advantages for assessing vegetation conditions across broad areas, its application in small to medium-scale regions faces challenges. These include low vegetation density and temporal mismatches arising from the spatial and temporal resolution limitations of satellite sensors such as MODIS, Landsat, and Sentinel (Zhou & Lyu, 2016). In recent years, visible and hyperspectral sensors have been integrated into UAV platforms for VC estimation due to their low cost, efficiency, ease of deployment, and precision (Fawcett *et al.*, 2020; Martínez *et al.*, 2021).

Furthermore, cutting-edge strategies in precision agriculture increasingly aim to develop more effective methods for monitoring and boosting crop production using UAV technology (Ahirwar *et al.*, 2019; Roslim *et al.*, 2021).

UAVs enable ultra-low-altitude flights ($<$100 m), capturing imagery with high spatial resolution ($\sim$10 cm), which facilitates the classification of bare soil, crops, and weeds. For such high-resolution imagery, it is essential to determine the VI that best enhances the contrast between vegetated and non-vegetated pixels. Several threshold-based segmentation algorithms are available for this purpose, including histogram mean, isodata, black pixel percentage, two peaks, Otsu, and Otsu-Valley methods. However, since UAV flights cannot be conducted continuously over time or across large areas, it becomes necessary to extrapolate VC data using vegetation indices derived from satellite sensors such as Sentinel-2. This allows for comprehensive spatial and temporal monitoring of VC throughout the crop cycle.

Therefore, the objective of this study was to calibrate maize crop VC using various vegetation indices derived from Sentinel-2 satellite imagery and to validate these estimates with multispectral images captured by a multispectral camera mounted on a UAV. Additionally, the VICAL tool was adapted to automate the estimation of VC.

MATERIALS AND METHODS

In this study, images acquired using a multispectral camera mounted on an Unmanned Aerial Vehicle (UAV) were employed to calculate the observed vegetation cover (VC). This observed VC was then correlated with various vegetation indices (VIs) to identify functional relationships that enable the indirect estimation of VC using Sentinel-2 satellite imagery. The simplified calibration methodology is illustrated in Figure 1.

Study area

The study area is located within the "Laguna de Bustillos" watershed, between coordinates 28° 29' 19"'N and 106° 58' 24" W, in a maize field equipped with a central pivot sprinkler irrigation system, covering an area of 54.28 hectares. The field is situated in Campo 2B of the Mennonite agricultural zone in Cuauhtémoc, Chihuahua, Mexico. Notably, the municipality of Cuauhtémoc ranked first in national maize production during the 2022 spring-summer agricultural cycle (SIAP, 2023). Two yellow maize hybrids, P1898 and P1445, were sown on April 13, 2023, at a planting density of 90,000 plants per hectare. The watershed is located in the northwestern part of the state of Chihuahua (Figure 2) and forms part of Hydrological Region No. 34, known as "Cuencas Cerradas del Norte". The prevailing climate in the region is semi-arid temperate, and the watershed's drainage network is radial, converging concentrically towards the lagoon —an indication that the basin is sustained primarily by rainfall (CONAGUA, 2024). According to data from the network of weather stations managed by the Unión de Fruticultores del Estado de Chihuahua (UNIFRUT), the average maximum temperature over the past year was 23.8 °C, while the average minimum was 6.5 °C. The annual average precipitation ranged between 390 and 400 mm (UNIFRUT, 2023).

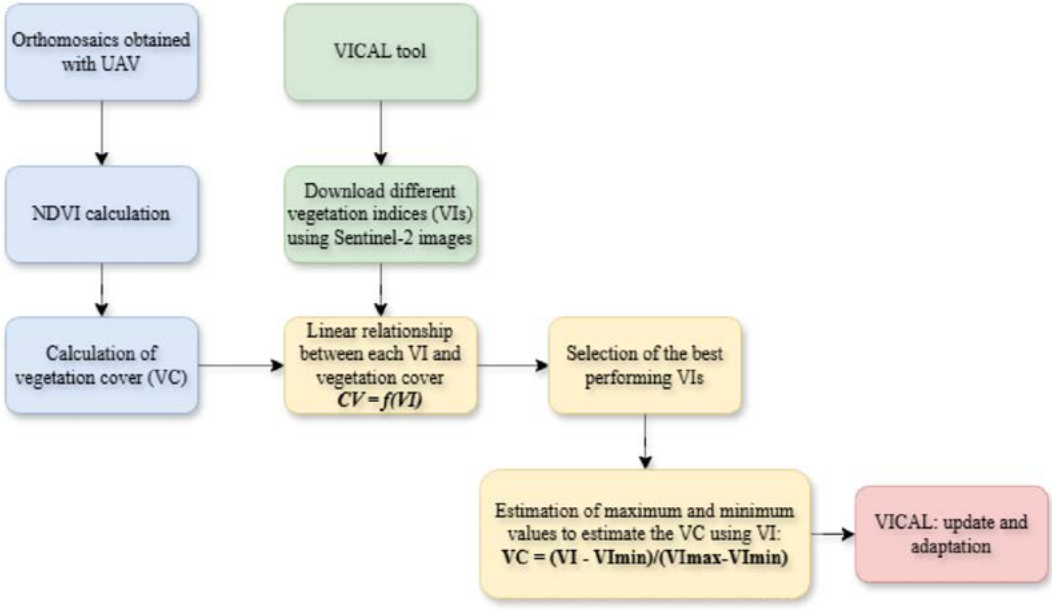

Figure 1. Flowchart of the methodology employed. The observed vegetation cover (VC) was obtained from georeferenced orthomosaics generated by a UAV.

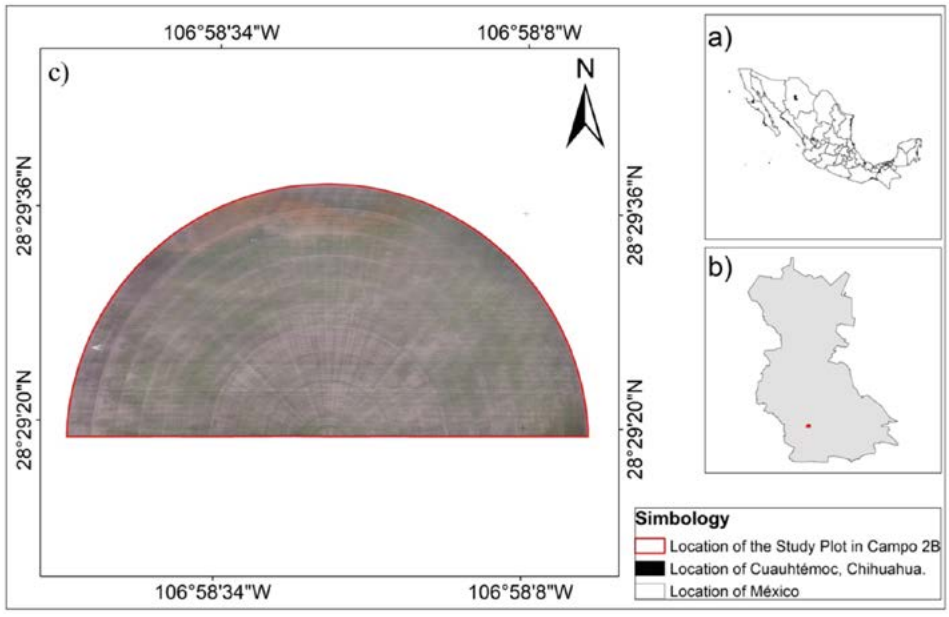

Figure 2. Study area: a) Location of Mexico, b) Location of the municipality of Cuauhtémoc, Chihuahua, and c) Location of the study plot in Campo 2B within the Mennonite agricultural zone in Ciudad Cuauhtémoc, Chihuahua, Mexico.

Meteorological data recorded during the 2023 agricultural cycle are presented in Figure 3. The average air temperature was 16.03 °C, with maximum and minimum averages of 24.62 °C and 7.43 °C, respectively. Solar radiation averaged 22.15 MJ m^{-2} day^{-1}, while the vapor pressure deficit (VPD) maintained an average of 0.93 kPa. Reference evapotranspiration (ETo) was calculated using the FAO56 Penman-Monteith method, resulting in an average of 4.33 mm, with peak values occurring in June and July coinciding with the crop's peak development stages. Total rainfall during the entire growing season amounted to 184.8 mm, indicating a precipitation deficit for the cycle. This underscores the importance of continuous monitoring of agricultural variables through remote sensing technologies.

Aerial image acquisition

During the 2023 spring summer agricultural cycle, multispectral images were acquired using a camera mounted on an Unmanned Aerial Vehicle (UAV) throughout the phenological development of the crop. The equipment used was a DJI Phantom 4 Multispectral quadcopter, equipped with a multispectral camera comprising six spectral sensors (Table 1). These include a ½ 9-inch CMOS RGB sensor for the visible spectrum and five monochromatic sensors for multispectral image capture. Additionally, the UAV features a solar irradiance sensor mounted on top, which measures real-time sunlight exposure, thereby enhancing the accuracy of the acquired multispectral imagery. The general specifications of the sensors are detailed in Table 1.

A total of 16 UAV flights were conducted (Table 2) between May and September 2023. The flights were scheduled for 12:00 p.m. local time, coinciding with the solar zenith,

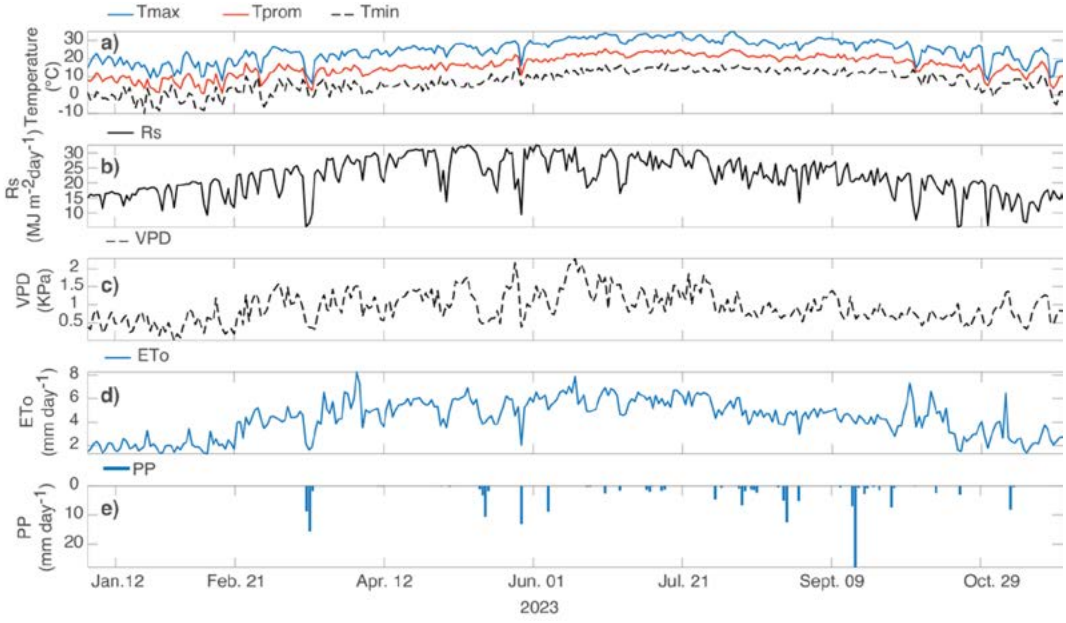

Figure 3. Meteorological data during the agricultural cycle of 2023. a) Tprom: Average air temperature (red line), Tmin: Minimum temperature (dashed black line), Tmax: Maximum temperature (blue line), b) Rs: Solar radiation (black line), c) VPD: Vapor pressure deficit (dashed black line), d) ETo: Reference evapotranspiration Pen-man Montieth method (blue line) and e) PP: precipitation (blue bars).

Table 1. Specifications of the UAV's multispectral camera.

Features	Description
Sensors	CMOS (RGB and 5-band multispectral)
Sensor Type	Global electronic shutter
Effective Pixels per Sensor	2.08 MP
Spectral Sensors	Blue (B): 450 nm ± 16 nm
Focal Length	Green (G): 560 nm ± 16 nm
Operating Temperature	Red (R): 650 nm ± 16 nm

and had an effective duration of approximately 25 to 27 minutes. The flight altitude was maintained at 60 meters above the plot, enabling a spatial resolution (Ground Sample Distance, GSD) of 10 cm/pixel. The processing of the multispectral images and the generation of georeferenced orthomosaics were carried out using the PIX4Dfields software.

Vegetation cover estimation

Vegetation cover (VC) is defined as the vertical representation of crop foliage over the soil surface, typically expressed as a percentage or fraction of the area (Choi *et al.*, 2016). During the early phenological stages of maize growth specifically the vegetative stage a greater number of pixels correspond to bare soil. As maize plants continue to develop, canopy cover progressively increases. Subsequently, during the reproductive development stage, canopy cover reaches its maximum extent, resulting in a gradually increasing number of pixels classified as vegetation. From the generated orthomosaics, the Normalized Difference Vegetation Index (NDVI) was calculated for each date.

Table 2. UAV flight dates and multispectral image acquisition.

Flight No.	Flight date	Wind speed (m/s)	Temperature (°C)	Days After Sowing (DAS)	Growing Degree Days (GDD)
1	06/05/2023	1.65	28.07	23	214.9
2	13/05/2023	3.01	26.21	30	251.3
3	20/05/2023	2.13	22.73	37	285.4
4	27/05/2023	1.88	27.74	44	348.3
5	03/06/2023	1.30	28.34	51	394.3
6	10/06/2023	2.22	30.01	58	452.5
7	19/06/2023	1.78	30.87	67	551.8
8	24/06/2023	1.81	33.07	72	611.8
9	08/07/2023	2.18	33.56	86	778.4
10	15/07/2023	2.10	31.42	93	867.9
11	22/07/2023	1.75	31.21	100	957.5
12	29/07/2023	2.18	29.93	107	1038.2
13	04/08/2023	0.77	32.22	113	1102.6
14	06/09/2023	1.22	31.01	146	1451.0
15	09/09/2023	1.01	31.08	149	1481.8
16	18/09/2023	5.34	26.61	158	1566.4

To distinguish vegetation from other land cover types, the approach proposed by Marcial-Pablo *et al.* (2019) was employed. This method relies on analyzing NDVI intensity histograms to determine a threshold value that classifies pixels as either crop (NDVI>threshold) or soil (NDVI<threshold). The threshold was calculated automatically using the Otsu-Valley thresholding algorithm (Hui-Fuang, 2006), which has demonstrated superior performance compared to the original Otsu method (Otsu, 1979) in recent studies involving RGB or multispectral imagery for precision agriculture (*e.g.*, Marcial-Pablo *et al.*, 2017). The Otsu method identifies an optimal threshold using a grayscale image histogram by satisfying two conditions: maximizing between-class variance and minimizing within-class weighted variance (Equation 1). Hui-Fuang (2006) introduced an enhancement to the original algorithm, known as the Otsu-Valley method. This improved technique determines the optimal threshold by locating the histogram value situated between the two highest peaks of the spectral histogram (Equation 2).

$$t^* = \underset{0 \le t < L}{ArgMax} \left\{ \omega_1(t)\left(\mu_1(t) - \mu_T\right) + \omega_2(t)\left(\mu_2(t) - \mu_T\right)^2 \right\} \quad (1)$$

$$t^* = \underset{0 \le t < L}{ArgMax} \left\{ \left(1 - p_t\right)\left(\omega_1(t)\,\mu_1^2(t) + \omega_2(t)\,\mu_2^2(t)\right) \right\} \quad (2)$$

Where t^* represents the optimal threshold, ω denotes the class probabilities, μ is the mean gray-level value of the respective classes, and $\mu_T<$ is the overall mean gray level of the entire image.

Based on the classification of vegetation pixels (derived using the NDVI index and the calculated threshold), the vegetation cover fraction for the study site was computed as the ratio between the area classified as vegetation and the total delineated area. The entire procedure was implemented in MATLAB.

Relationship between vegetation indices and vegetation cover

The estimation of agronomic variables in maize is commonly based on one or two vegetation indices (VIs), with the most prevalent being the Soil-Adjusted Vegetation Index (SAVI) and the Normalized Difference Vegetation Index (NDVI). However, access to advanced technologies such as Google Earth Engine (GEE) has facilitated the acquisition and processing of a larger number of VIs, enabling a more comprehensive and diversified analysis of the phenomenon under study.

In this work, a total of 16 vegetation indices were calculated (Table 3) using Sentinel-2 satellite imagery. The VI values were automatically extracted through the Google Earth Engine platform using the VICAL tool (Vegetation Index Calculator, Jiménez-Jiménez *et al.*, 2022).

Subsequently, linear regression models were employed to estimate the relationship between the vegetation indices (VIs) listed in Table 3 and the vegetation cover derived from the orthomosaics. A linear model was chosen due to its simplicity, ease of interpretation, and practical applicability —particularly beneficial for end-users such as technicians and agricultural producers. Accordingly, the coefficient of determination (R^2, Equation 3) was calculated, and the three VIs with the highest R^2 values were selected, in addition to the NDVI.

$$R^2 = 1 - \frac{\sum_{t=1}^{n}\left(y_t - \hat{y}_t\right)^2}{\sum_{t=1}^{n}\left(y_t - \bar{y}_t\right)^2} \tag{3}$$

Where y_t represents the measured values, $\hat{y}_t$ the estimated values, and $\bar{y}_t$ the actual mean value.

Based on the four selected vegetation indices, the maximum and minimum values required to estimate vegetation cover (VC) were determined using the model proposed by Hunsaker *et al.* (2005) (Equation 4).

$$VC = \frac{VI - VI_{\min}}{VI_{\max} - VI_{\min}} \tag{4}$$

Where: VI is the mean value of the vegetation index; $VI_{\max}$ is the maximum value of the vegetation index (VI) when the crop reaches its maximum ground cover and $VI_{\min}$ is the value of the VI of the bare soil.

Table 3. Vegetation indices used for vegetation cover estimation (adapted from Jiménez-Jiménez *et al.*, 2022).

Number	Vegetation index	Equation	Reference
1	Atmospherically resistant vegetation index	$ARVI = \frac{NIR-(R-\gamma(B-R))}{NIR+(R-\gamma(B-R))}$ $\gamma=1.0$	Kaufman & Tanré, 1992
2	Adjusted transformed soil-adjusted vegetation index	$ATSAVI = \frac{[a(NIR-aR-b)]}{[(R+aNIR-ab+X(1+a^2))]}$ $a=1$; $b=0$; $X=0.08$	Baret & Guyot, 1991
3	Difference vegetation index	$DVI = NIR\text{-}R$	Richardson & Wiegand, 1977)
4	Enhanced vegetation index	$EVI = 2.5\left(\frac{NIR-R}{NIR+6R-7.5B+1}\right)$	A. Huete *et al.*, 2002
5	Enhanced vegetation index	$EVI2 = 2.5\left(\frac{NIR-R}{NIR+2.4R+1}\right)$	Jiang *et al.*, 2008
6	Green normalized difference vegetation index	$GNDVI = \frac{NIR-G}{NIR+G}$	Gitelson *et al.*, 1996
7	Modified soil adjusted vegetation index	$MSAVI2 = \frac{(2NIR+1)-\sqrt{(2NIR+1)^2-8(NIR-R)}}{2}$	Qi *et al.*, 1994
8	Modified triangular vegetation index	$MTVI = 1.2[1.2(NIR-G)-2.5(R-G)]$	Haboudane *et al.*, 2004
9	Modified triangular vegetation index-2	$MTVI2 = \frac{1.5[1.2(NIR-G)-2.5(R-G)]}{\sqrt{(2NIR+1)^2-(6NIR-5\sqrt{R})-0.5}}$	Haboudane *et al.*, 2004
10	Normalized difference vegetation index	$NDVI = \frac{NIR-R}{NIR+R}$	Rouse *et al.*, 1973
11	Optimized soil adjusted vegetation index	$OSAVI = 1.16\left(\frac{NIR-R}{NIR+R+X}\right)$ $X=0.16$	Rondeaux *et al.*, 1996
12	Renormalized difference vegetation index	$RDVI = \frac{NIR-R}{\sqrt{NIR+R}}$	Roujean & Breon, 1995
13	Soil adjusted vegetation index	$SAVI = \frac{NIR-R}{NIR+R*L}(1+L)$ $L=0.5$	A. R. Huete, 1988
14	Triangular vegetation index	$TVI = 0.5[120(NIR-G)-200(R-G)]$	Broge & Leblanc, 2001
15	Transformed soil adjusted vegetation index	$TSAVI = \frac{[a(NIR-aR-b)]}{[(R+aNIR-ab)]}$ $a=1$; $b=0$;	Baret *et al.*, 1989
16	Wide dynamic range vegetation index	$WDRVI = \frac{0.2NIR-R}{0.2NIR+R}$	(Gitelson, 2004)

*R: Red band, G: Green band, B: Blue band, NIR: Near-infrared band.

Error parameters

To statistically evaluate the model and compare performance, the following metrics were used: Mean Error (ME), Mean Absolute Percentage Error (MAPE), Root Mean Square Error (RMSE), and the Coefficient of Determination (R^2) (Chicco *et al.*, 2021). Within this set of metrics, RMSE reflects the weighted variance of the errors, where lower values indicate higher precision; MAPE quantifies the average absolute percentage error; and R^2 represents the proportion of variance in the dependent variable that is predictable from the independent variables.

$$ME = \frac{1}{n}\sum_{t=1}^{n} y_t - \hat{y}_t \tag{5}$$

$$MAPE = \frac{1}{n}\sum_{t=1}^{n}\left|\frac{y_t - \hat{y}_t}{y_t}\right| \times 100 \tag{6}$$

$$RMSE = \sqrt{\frac{1}{n}\sum_{t=1}^{n}\left(y_t - \hat{y}_t\right)^2} \tag{7}$$

RESULTS AND DISCUSSION

Vegetation cover

Figure 4 illustrates the dynamics of vegetation cover (VC) during the vegetative growth period, starting with values of 0.1 at 23 Days After Sowing (DAS) (~214.9 Growing Degree Days, GDD), followed by gradual increases reaching 0.2 at 51 DAS (~394.3 GDD). After this stage, a rapid increase is observed, culminating in approximately 867.9 GDD (93 DAS) with a VC value of 0.8. This value is characteristic of row-planted crops, which typically do not exceed 90% VC (Imukova *et al.*, 2015). During this period, the crop reaches maximum leaf greenness shortly after flowering (Valentinuz and Tollenaar,

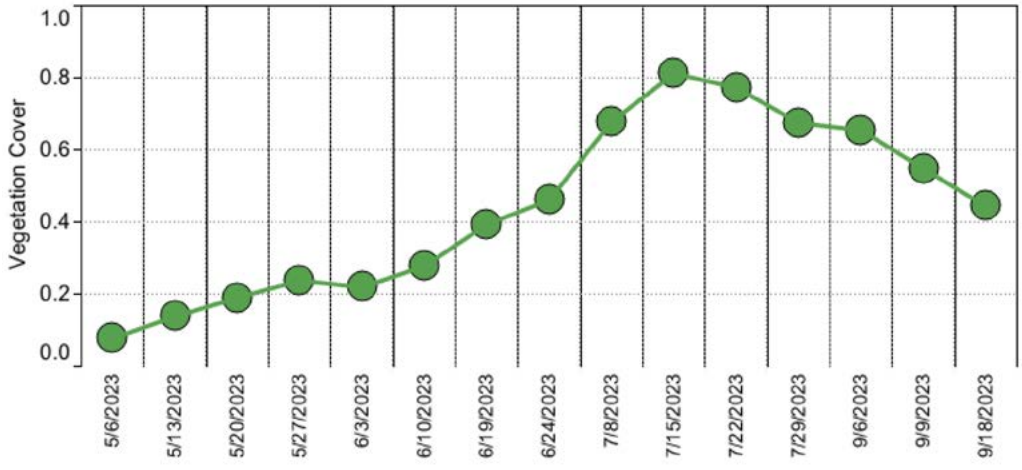

Figure 4. Vegetation cover values on UAV flight dates during the phenological development of maize.

2004). Subsequently, VC values begin to gradually decline throughout the reproductive stage and into senescence, reaching values around 0.4. This trend is closely linked to the crop's phenological stages and canopy density (You *et al.*, 2013; Marcial-Pablo *et al.*, 2019). Moreover, accurate estimation of VC is crucial for quantifying surface processes, including hydrological fluxes in agricultural lands (Jung *et al.*, 2006), as well as understanding annual vegetation development dynamics.

Figure 5 illustrates the temporal evolution of vegetation cover (VC) during the maize crop growth stages. The first UAV flight, conducted on May 6, 2023, at 23 Days After Sowing (DAS), recorded a VC of 8% within the plot. By the second flight, on May 13 (30 DAS), the VC had increased to 14%. From flights 3 to 6, conducted between May 20 and June 10 at 37, 44, 51, and 58 DAS respectively, a similar spatial pattern was observed, with VC values of 19%, 24%, 22%, and 28%.

As the crop developed, VC continued to increase, with the northern section of the plot consistently showing the highest coverage. García-Martínez *et al.* (2020) indicated that this spatial variability may be attributed to factors such as the plant material used, sowing date, soil type, irrigation practices, fertilization, rainfall, and planting density.

On June 19 and 24 (67 and 72 DAS), VC rose to 39% and 46%, respectively, showing a more uniform spatial distribution across the field. By July 8 (86 DAS), VC reached 68%. On July 15 (93 DAS), VC peaked at 81%, indicating a near-complete canopy closure. At this stage, the crop was at its most vigorous vegetative development, a result of the continuous accumulation of nutrients primarily nitrogen which is closely associated with biomass growth (Ji *et al.*, 2021).

From July 22 to September 18 (100 to 158 DAS), VC gradually declined from 77% to 44%, due to the natural process of leaf senescence (Abeledo *et al.*, 2020).

Vegetation index calibration

Based on the analysis of vegetation cover (VC) and its relationship with various vegetation indices (VIs), a strong linear correlation was observed between VC and the majority of the VIs, with most presenting an $R^2>0.9$. The three indices with the highest R^2 values (Figure 6) were the Atmospherically Resistant Vegetation Index (ARVI, $R^2=0.963$), the Enhanced Vegetation Index (EVI, $R^2=0.963$), and the Optimized Soil-Adjusted Vegetation Index (OSAVI, $R^2=0.960$), all of which exhibited slightly better performance than the NDVI (Normalized Difference Vegetation Index, $R^2=0.945$) in representing vegetation cover.

This trend has also been reported in other studies, where indices such as OSAVI have demonstrated superior performance over NDVI in estimating VC (He *et al.*, 2019).

The maximum and minimum values for these vegetation indices are presented in Figure 7. According to the error parameters shown in this figure, the Atmospherically Resistant Vegetation Index (ARVI) can be reliably used to monitor vegetation cover (VC) with high precision for forage maize in Cuauhtémoc, Chihuahua, provided that the specified maximum and minimum index values are applied. ARVI yielded a Root Mean Square Error (RMSE) of 0.7, indicating a strong predictive performance.

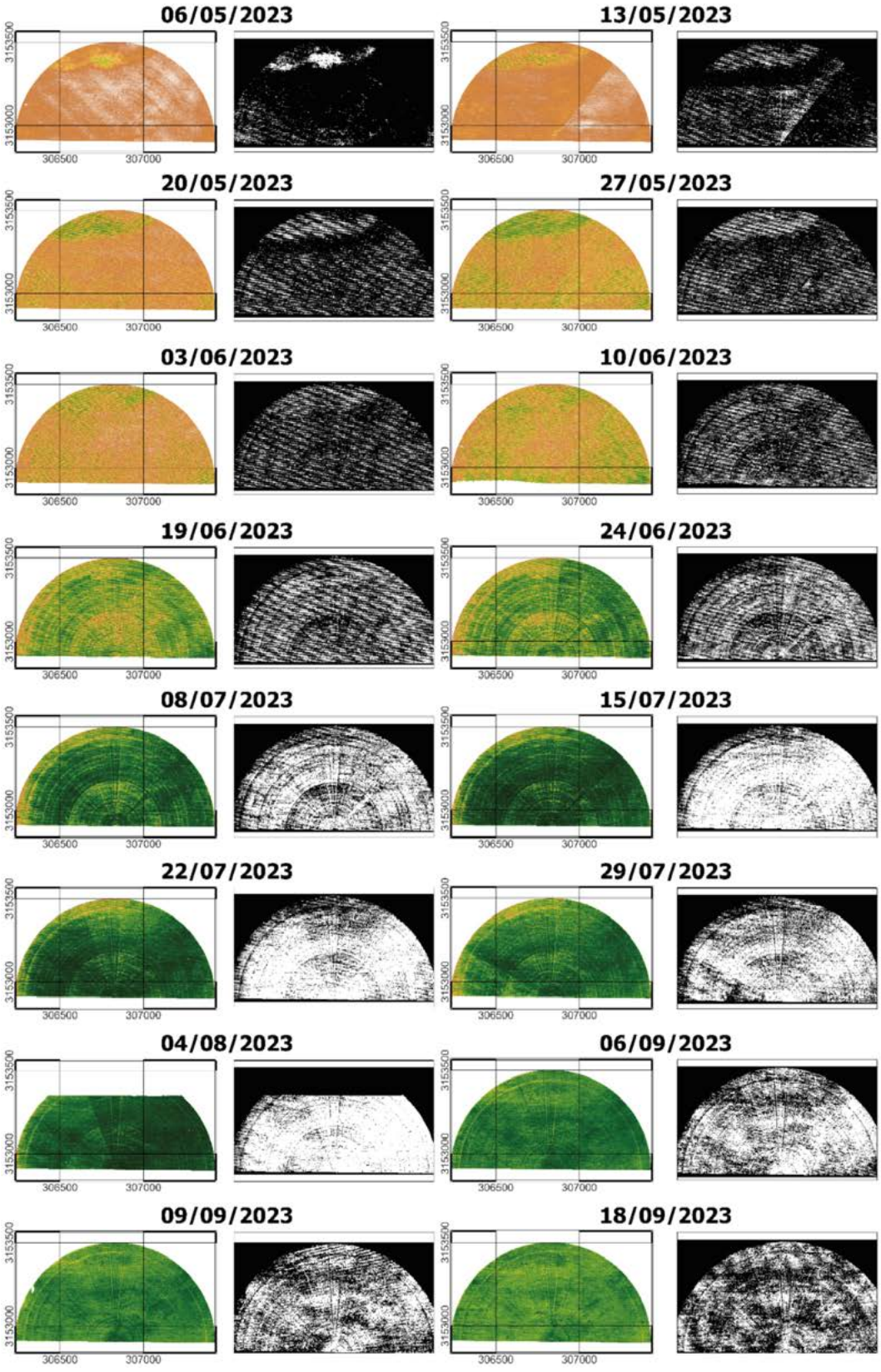

Figure 5. Vegetation cover classification on the UAV flight dates.

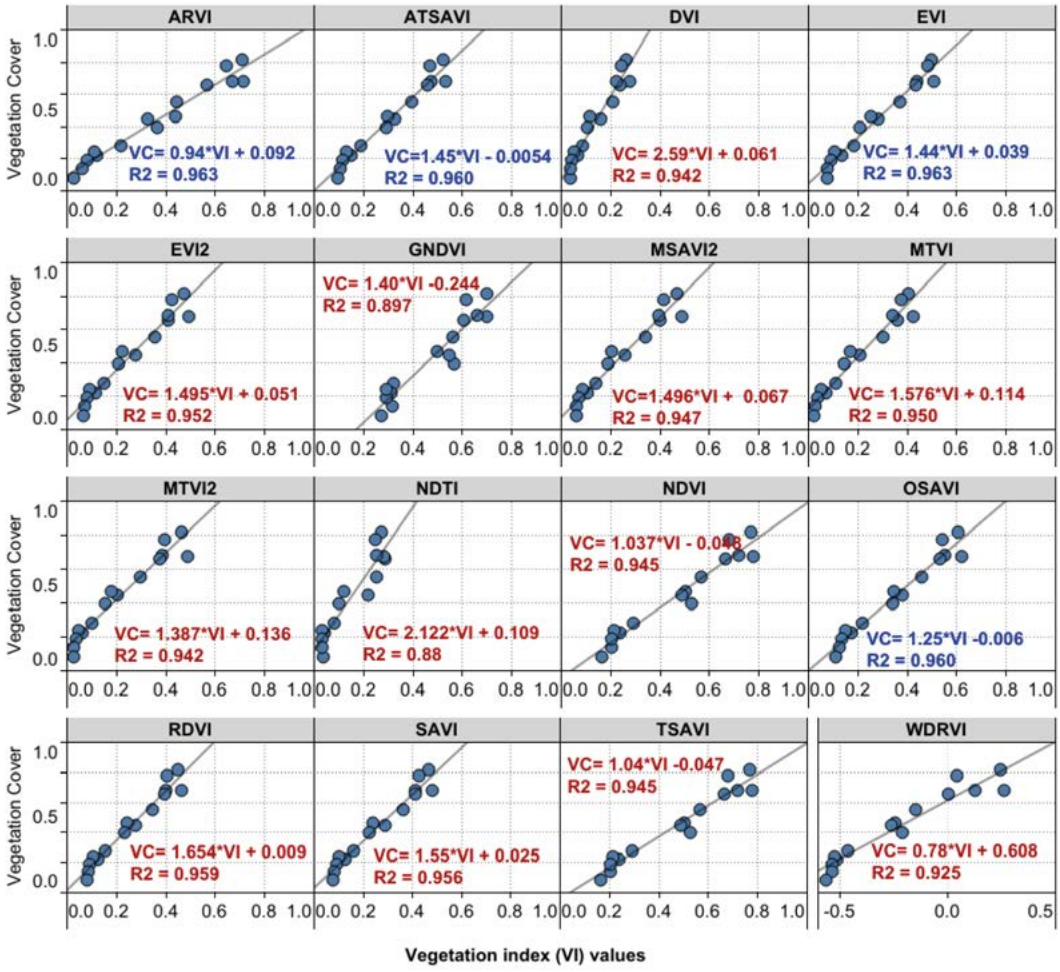

Figure 6. Relationship between vegetation cover and vegetation indices.

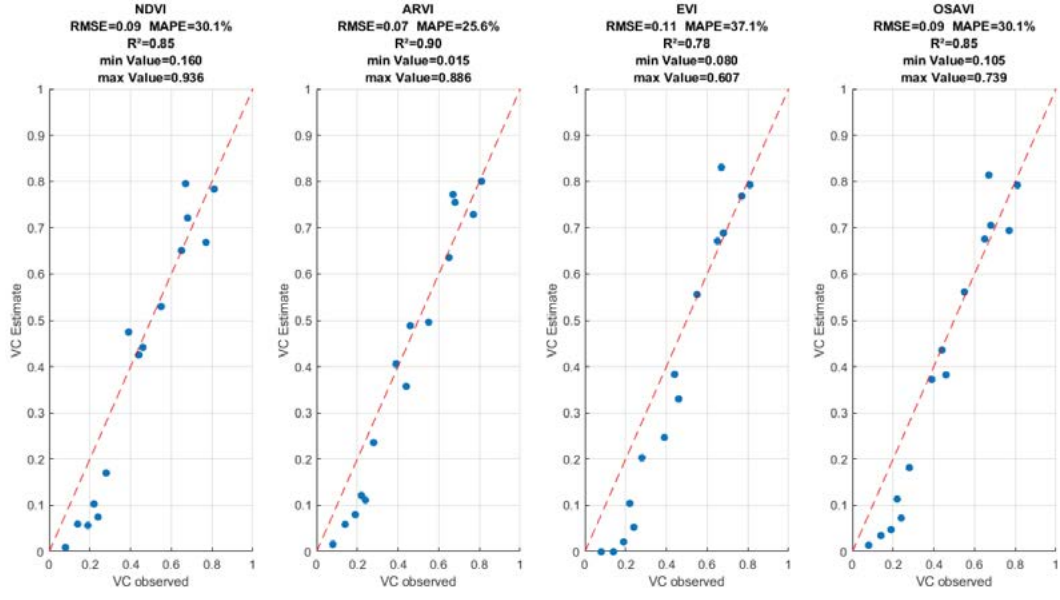

Figure 7. Vegetation cover estimated using vegetation indices.

ARVI has been shown to be less sensitive to atmospheric conditions compared to NDVI (Bannari *et al.*, 1995; Almalki *et al.*, 2022).

VICAL Adaptation to estimate vegetation cover

To automate vegetation cover estimation using VIs, the VICAL tool was adapted (https://inifapcenidraspa.users.earthengine.app/view/vical, Jiménez-Jiménez *et al.*, 2022). This adaptation includes: i) using equation 4 to estimate VC, ii) the ability to enter the VI_{min} and VI_{max} values indicated in Figure 7 for the ARVI, as well as defining the interval from 0 to 1 to represent the VC range (Figure 8). This functionality allows for automated (Figure 8a) and continuous (Figure 8b) monitoring of vegetation cover, eliminating the need to use spreadsheets or other external image analysis tools.

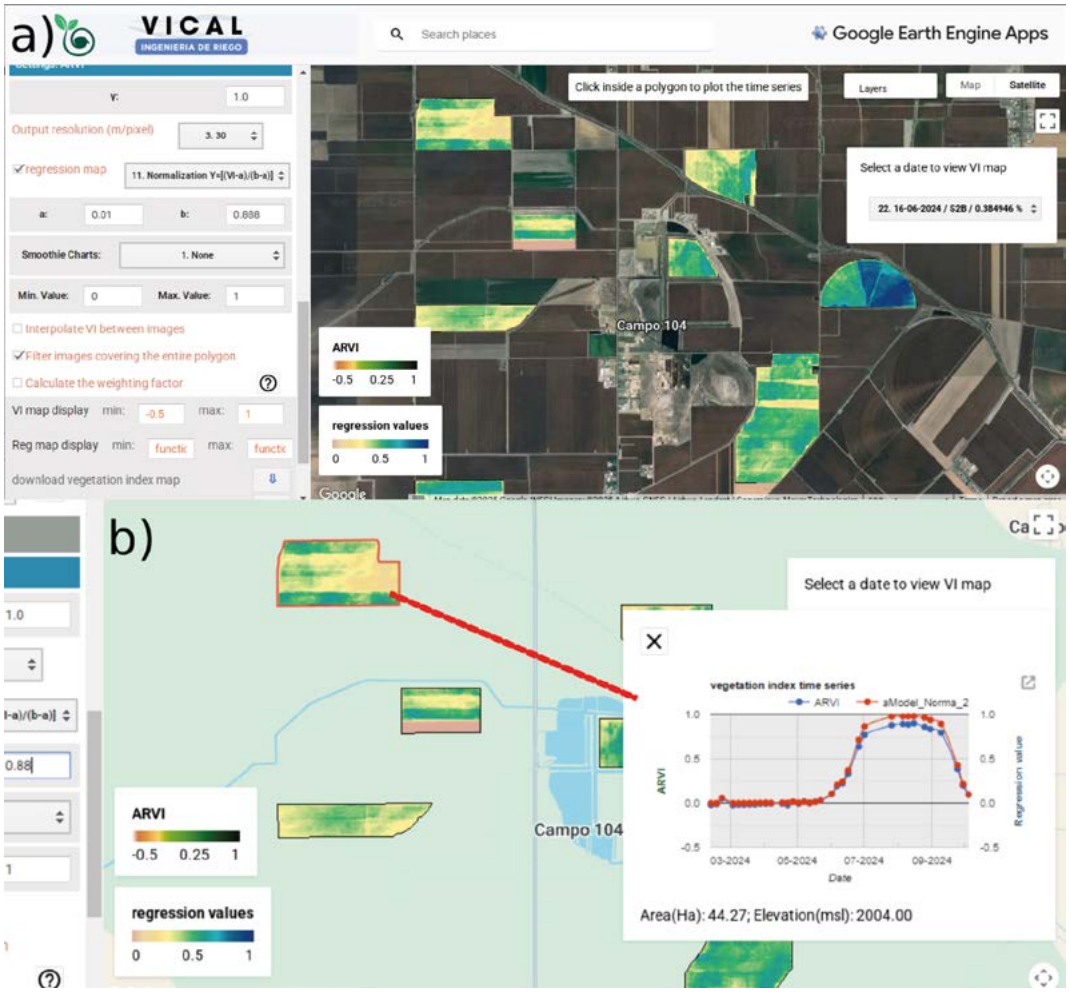

Figure 8. Adaptation of VICAL for vegetation cover (image date: June 16, 2024). a) Vegetation cover estimation using the ARVI index on corn plots in Cuauhtémoc (VICAL vector file ID: projects/ee-serchjimenez1990/assets/SHAPE_MAIZ_VICAL), Chihuahua; b) vegetation cover time series (red line graph) for the plot with a red border.

CONCLUSIONS

Three of the 16 vegetation indices showed acceptable performance: ARVI, NDVI, and OSAVI. Furthermore, the VC calculation was successfully introduced into the VICAL database, allowing for reliable and automatic calculation of vegetation cover for corn crops. This proposed methodology allows for quick and easy calibration of vegetation cover, along with other agricultural variables, using satellite information; it can also be replicated in other areas with prior calibration.

REFERENCES

Abeledo, L. G., Savin, R., & Slafer, G. A. (2020). Maize senescence under contrasting source-sink ratios during the grain filling period. *Environmental and Experimental Botany*, 180, 104263. doi.org/10.1016/j.envexpbot.2020.104263

Ahirwar, S., Swarnkar, R., Bhukya, S., & Namwade, G. (2019). Application of drone in agriculture. *International Journal of Current Microbiology and Applied Sciences, 8*(01), 2500-2505. doi.org/10.20546/ijcmas.2019.801.264

Allen, R.G., Pereira, L.S., Raes, D., Smith, M., (1998). Crop evapotranspiration: Guidelines for computing crop requirements. *Irrigation and Drainage Paper* No. 56, FAO. https://doi.org/10.1016/j.eja.2010.12.001

Almalki, R., Khaki, M., Saco, P. M., & Rodriguez, J. F. (2022). Monitoring and mapping vegetation cover changes in arid and semi-arid areas using remote sensing technology: A review. *Remote Sensing, 14*(20), 5143. doi.org/10.3390/rs14205143

Alonso, H., Diakite, L., & Rufino, J. (2020). Impacto del cambio de cobertura vegetal y del clima en la erosión del Nevado de Toluca. *Tecnología y ciencias del agua, 11*(3), 342-370. doi.org/10.24850/j-tyca-2020-03-10

Bannari, A., Morin, D., Bonn, F., & Huete, A. (1995). A review of vegetation indices. *Remote sensing reviews, 13*(1-2), 95-120. doi.org/10.1080/02757259509532298

Baret, F. (1989). TSAVI: a vegetation index which minimizes soil brightness effects on LAI and APAR estimation. In 12th Canadian Symp. on Remote Sensing and IGARSS'90, Vancouver, Canada, 10-14 July 1989.

Baret, F., & Guyot, G. (1991). Potentials and limits of vegetation indices for LAI and APAR assessment. *Remote sensing of environment, 35*(2-3), 161-173. doi.org/10.1016/0034-4257(91)90009-U

Broge, N. H., & Leblanc, E. (2001). Comparing prediction power and stability of broadband and hyperspectral vegetation indices for estimation of green leaf area index and canopy chlorophyll density. *Remote sensing of environment, 76*(2), 156-172. doi.org/10.1016/S0034-4257(00)00197-8

Calera, A. B. (2005). La evapotranspiración: concepto y metodología de cálculo. Agua y Agronomía.1re edición. Editorial: Mudi-Prensa. Barcelona, España. 163-238.

Chicco, D., Warrens, M. J., & Jurman, G. (2021). The coefficient of determination R-squared is more informative than SMAPE, MAE, MAPE, MSE and RMSE in regression analysis evaluation. *Peerj computer science*, 7, e623. doi.org/10.7717/peerj-cs.623

Choi, S. K., Lee, S. K., Jung, S. H., Choi, J. W., Choi, D. Y., & Chun, S. J. (2016). Estimation of fractional vegetation cover in sand dunes using multi-spectral images from fixed-wing UAV. *Journal of the Korean Society of Surveying, Geodesy, Photogrammetry and Cartography, 34*(4), 431-441. doi.org/10.7848/ksgpc.2016.34.4.431

CONAGUA. 2024. Comisión Nacional del Agua. Obtenido de https://sigagis.conagua.gob.mx/gas1/Edos_Acuif eros_18/chihuahua/DR_0805.pdf

Fawcett, D., Panigada, C., Tagliabue, G., Boschetti, M., Celesti, M., Evdokimov, A., ... & Anderson, K. (2020). Multi-scale evaluation of drone-based multispectral surface reflectance and vegetation indices in operational conditions. *Remote sensing, 12*(3), 514. doi.org/10.3390/rs12030514

Fern, R. R., Foxley, E. A., Bruno, A., & Morrison, M. L. (2018). Suitability of NDVI and OSAVI as estimators of green biomass and coverage in a semi-arid rangeland. *Ecological Indicators*, 94, 16-21. doi.org/10.1016/j.ecolind.2018.06.029

García-Martínez, H., Flores-Magdaleno, H., Khalil-Gardezi, A., Ascencio-Hernández, R., Tijerina-Chávez, L., Vázquez-Peña, MA, & Mancilla-Villa, OR (2020). Estimación de la fracción de cobertura de la vegetación en maíz (*Zea mays*) mediante imágenes digitales tomadas por un vehículo aéreo no tripulado (UAV). *Revista fitotecnia mexicana, 43*(4), 399-409. doi.org/10.35196/rfm.2020.4.399

Gitelson, A. A., Kaufman, Y. J., & Merzlyak, M. N. (1996). Use of a green channel in remote sensing of global vegetation from EOS-MODIS. *Remote sensing of Environment, 58*(3), 289-298. doi.org/10.1016/S0034-4257(96)00072-7

Gitelson, A. A. (2004). Wide dynamic range vegetation index for remote quantification of biophysical characteristics of vegetation. *Journal of plant physiology, 161*(2), 165-173. doi.org/10.1078/0176-1617-01176

Gonsamo, A., D'odorico, P., & Pellikka, P. (2013). Measuring fractional forest canopy element cover and openness–definitions and methodologies revisited. *Oikos, 122*(9), 1283-1291. doi.org/10.1111/j.1600-0706.2013.00369

Haboudane, D., Miller, J. R., Pattey, E., Zarco-Tejada, P. J., & Strachan, I. B. (2004). Hyperspectral vegetation indices and novel algorithms for predicting green LAI of crop canopies: Modeling and validation in the context of precision agriculture. *Remote sensing of environment, 90*(3), 337-352. doi.org/10.1016/j.rse.2003.12.013

He, J., Zhang, N., Su, X., Lu, J., Yao, X., Cheng, T., ... & Tian, Y. (2019). Estimating leaf area index with a new vegetation index considering the influence of rice panicles. *Remote Sensing, 11*(15), 1809. doi.org/10.3390/rs11151809

Hui-Fuang, N. (2006). Automatic thresholding for defect detection. *Pattern recognition letters, 27*(14), 1644-1649. doi.org/10.1016/j.patrec.2006.03.009

Huete, A. R. (1988). A soil-adjusted vegetation index (SAVI). *Remote Sensing of Environment, 25*(3), 295-309. doi.org/10.1016/0034-4257(88)90106-X

Huete, A., Didan, K., Miura, T., Rodriguez, E. P., Gao, X., & Ferreira, L. G. (2002). Overview of the radiometric and biophysical performance of the MODIS vegetation indices. *Remote Sensing of Environment, 83*(1-2), 195-213. doi.org/10.1016/S0034-4257(02)00096-2

Hunsaker, D. J., Pinter, P. J., & Kimball, B. A. (2005). Wheat basal crop coefficients determined by normalized difference vegetation index. *Irrigation Science*, 24, 1-14. doi.org/10.1007/s00271-005-0001-0

Imukova, K., Ingwersen, J., & Streck, T. (2015). Determining the spatial and temporal dynamics of the green vegetation fraction of croplands using high-resolution RapidEye satellite images. *Agricultural and Forest Meteorology*, 206, 113-123. doi.org/10.1016/j.agrformet.2015.03.003

Ji, Z., Pan, Y., Zhu, X., Wang, J., & Li, Q. (2021). Prediction of crop yield using phenological in-formation extracted from remote sensing vegetation index. *Sensors, 21*(4), 1406. doi.org/10.3390/s21041406

Jiang, Z., Huete, A. R., Didan, K., & Miura, T. (2008). Development of a two-band enhanced vegetation index without a blue band. *Remote Sensing of Environment, 112*(10), 3833-3845. doi.org/10.1016/J.RSE.2008.06.006

Jiménez-Jiménez, S. I., Marcial-Pablo, M. D. J., Ojeda-Bustamante, W., Sifuentes-Ibarra, E., Inzunza-Ibarra, M. A., & Sánchez-Cohen, I. (2022). VICAL: global calculator to estimate vegetation indices for agricultural areas with landsat and sentinel-2 data. *Agronomy, 12*(7), 1518. doi.org/10.3390/agronomy12071518

Jung, M., Henkel, K., Herold, M., & Churkina, G. (2006). Exploiting synergies of global land cover products for carbon cycle modeling. *Remote Sesing of Environment, 101*(4), 534-553. doi.org/10.1016/j.rse.2006.01.020

Kaufman, Y. J., & Tanre, D. (1992). Atmospherically resistant vegetation index (ARVI) for EOS-MODIS. *IEEE transactions on Geoscience and Remote Sensing, 30*(2), 261-270. doi.org/10.1109/36.134076

Leirana-Alcocer, J. L., & Bautista-Zúñiga, F. (2014). Patrones de asociación entre la cobertura vegetal y la calidad del suelo en el matorral costero de la reserva Ría Lagartos, Yucatán. *Ciencia UAT, 8*(2), 44-53.

Marcial-Pablo, M. D. J., Gonzalez-Sanchez, A., Jimenez-Jimenez, S. I., Ontiveros-Capurata, R. E., & Ojeda-Bustamante, W. (2019). Estimation of vegetation fraction using RGB and multispectral images from UAV. *International journal of remote sensing, 40*(2), 420-438. doi.org/10.1080/01431161.2018.1528017

Marcial Pablo, M. J., Ojeda Bustamante, W., González Sánchez, A., & Jiménez Jiménez, S. (2017). Estimación de la cobertura vegetal usando imágenes RGB obtenidas desde un dron. III Congreso Nacional de riego y drenaje COMEII 2017. COMEI-17048.

Marcial-Pablo, M. D. J., Ontiveros-Capurata, R. E., Jimenez-Jimenez, S. I., & Ojeda-Bustamante, W. (2021). Maize crop coefficient estimation based on spectral vegetation indices and vegetation cover fraction derived from UAV-based multispectral images. *Agronomy, 11*(4), 668. doi.org/10.3390/agronomy11040668

Martinez, J. L., Lucas-Borja, M. E., Plaza-Alvarez, P. A., Denisi, P., Moreno, M. A., Hernández, D., ... & Zema, D. A. (2021). Comparison of satellite and drone-based images at two spatial scales to evaluate vegetation regeneration after post-fire treatments in a mediterranean forest. *Applied Sciences, 11*(12), 5423. doi.org/10.3390/app11125423

Ng, H. F. (2006). Automatic thresholding for defect detection. *Pattern recognition letters, 27*(14), 1644-1649. doi.org/10.1016/j.patrec.2006.03.009

Otsu, N. (1975). A threshold selection method from gray-level histograms. *Automatica, 11*(285-296), 23-27.

Qi, J., Chehbouni, A., Huete, A. R., Kerr, Y. H., & Sorooshian, S. (1994). A modified soil adjusted vegetation index. *Remote sensing of environment, 48*(2), 119-126. doi.org/10.1016/0034-4257(94)90134-1

Richardson, A. J., & Wiegand, C. L. (1977). Distinguishing vegetation from soil background information. *Photogrammetric engineering and remote sensing, 43*(12), 1541-1552.

Rondeaux, G., Steven, M., & Baret, F. (1996). Optimization of soil-adjusted vegetation indices. *Remote sensing of environment, 55*(2), 95-107. doi.org/10.1016/0034-4257(95)00186-7

Roslim, M. H. M., Juraimi, A. S., Che'Ya, N. N., Sulaiman, N., Manaf, M. N. H. A., Ramli, Z., & Motmainna, M. (2021). Using remote sensing and an unmanned aerial system for weed management in agricultural crops: A review. *Agronomy, 11*(9), 1809. doi.org/10.3390/agronomy11091809

Rouse Jr, J. W., Haas, R. H., Schell, J. A., & Deering, D. W. (1973). Monitoring the vernal advancement and retrogradation (green wave effect) of natural vegetation (No. NASA-CR-132982).

Roujean, J. L., & Breon, F. M. (1995). Estimating PAR absorbed by vegetation from bidirectional reflectance measurements. *Remote sensing of Environment, 51*(3), 375-384. doi.org/10.1016/0034-4257(94)00114-3

Sahoo, P. K., Soltani, S. A. K. C., & Wong, A. K. (1988). A survey of thresholding techniques. *Computer vision, graphics, and image processing, 41*(2), 233-260. doi.org/10.1016/0734-189X(88)90022-9

SIAP. 2022. Servicio de Información Agroalimentaria y Pesquera Estimación de Superficie Agrícola P-V 2022 Chihuahua 2023. Obtenido de https://www.gob.mx/cms/uploads/atta-ment/file/821520/ESA_Chihuahua_PV_2022.pdf

Torres-Sánchez, J., Pena, J. M., de Castro, A. I., & López-Granados, F. (2014). Multi-temporal mapping of the vegetation fraction in early-season wheat fields using images from UAV. *Computers and Electronics in Agriculture*, 103, 104-113. doi.org/10.1016/j.compag.2014.02.009

UNIFRUT. 2023. Unión Agrícola Regional de Fruticultores del Estado de Chihuahua A.C. Obtenido de https://www.unifrut.com.mx/rem/rem.php

Valentinuz, O. R., & Tollenaar, M. (2004). Vertical profile of leaf senescence during the grain'filling period in older and newer maize hybrids. *Crop Science, 44*(3), 827-834. doi.org/10.2135/cropsci2004.8270

Xiao, J., & Moody, A. (2005). A comparison of methods for estimating fractional green vegetation cover within a desert-to-upland transition zone in central New Mexico, USA. *Remote sensing of environment, 98*(2-3), 237-250. doi.org/10.1016/j.rse.2005.07.011

Xue, J., & Su, B. (2017). Significant remote sensing vegetation indices: A review of developments and applications. *Journal of sensors*, 2017(1), 1353691. doi.org/10.1155/2017/1353691

Yang, C., Everitt, J. H., & Bradford, J. M. (2006). Comparison of QuickBird satellite imagery and airborne imagery for mapping grain sorghum yield patterns. *Precision Agriculture*, 7, 33-44. doi.org/10.1007/s11119-005-6788-0

You, X., Meng, J., Zhang, M., & Dong, T. (2013). Remote sensing based detection of crop phenology for agricultural zones in China using a new threshold method. *Remote Sensing, 5*(7), 3190-3211. doi.org/10.3390/rs5073190

Yu, Z., Cao, Z., Wu, X., Bai, X., Qin, Y., Zhuo, W., ... & Xue, H. (2013). Automatic image-based detection technology for two critical growth stages of maize: Emergence and three-leaf stage. *Agricultural and forest meteorology*, 174, 65-84. doi.org/10.1016/j.agrformet.2013.02.011

Zhou, L., & Lyu, A. (2016). Investigating natural drivers of vegetation coverage variation using MODIS imagery in Qinghai, China. *Journal of Arid Land, 8*(1), 109-124. doi.org/10.1007/s40333-015-0016-1